Eur. Phys. J. B **5**, 839–846 (1998)

THE EUROPEAN PHYSICAL JOURNAL B

The phonon dispersion in 6H-SiC investigated by inelastic neutron scattering

B. Dorner[1,a], H. Schober[1], A. Wonhas[1], M. Schmitt[2], and D. Strauch[2]

[1] Institut Laue-Langevin, 38042 Grenoble, France
[2] Institut für Theoretische Physik, Universität Regensburg, 93040 Regensburg, Germany

Received: 28 April 1998 / Accepted: 15 June 1998

Abstract. Using coherent inelastic neutron scattering we have investigated the phonon dispersion relation of bulk hexagonal 6H-SiC. The complete set of phonon branches has been determined along the $\Gamma-A$ and 14 out of 36 branches along the $\Gamma-M$ direction. The experimental data are compared to *ab initio* calculations for cubic 3C-SiC transposed to 6H-SiC. Good agreement between theory and experiment is found for the $\Gamma-A$ direction. The discrepancies encountered for the $\Gamma-M$ direction are interpreted as evidence for a dependence of the dynamical response in the SiC system on the stacking sequence.

PACS. 63.20.-e Phonons in crystal lattices – 78.70.Nx Neutron inelastic scattering

1 Introduction

Silicon carbide (SiC) is a semiconductor with remarkable chemical, thermal and mechanical stability. It is a promising candidate for a broad variety of applications such as high-power, high-speed, and high-frequency devices which can be operated under extreme environmental conditions, *e.g.*, high temperatures or high radiation [1]. These conditions cannot be met by classical semiconductors. In view of these perspectives, the basic physical properties of this material should be studied in as much detail as possible. The knowledge of the phonon dispersion curves provides the most direct information on the lattice dynamics, *i.e.*, the (harmonic part of the) interatomic potential. The dispersion relations are an essential input for the calculation of other phonon-related properties such as the specific heat, thermal expansion, heat conductivity, *etc.* Moreover, phonon dispersion curves reflect the structure of a material, and in the case of SiC they may add to the insight into its polytypism. SiC is able to develop a large variety of stable, long-range ordered structures [2]. Up to now, more than 100 distinct polytypes have been identified [3,4]. Since the electronic contributions to the free energy of various polytypes differ by only extremely small amounts [5], the role of phonons in stabilizing certain phases has been a matter of theoretical investigation [6].

Despite of the technical relevance of the material little is known experimentally about its lattice-dynamical properties. Since the Raman results of Feldman *et al.* [7] and the preliminary inelastic neutron-scattering (INS) data of Lorenz *et al.* [8] no major experimental investigation of the phonon-dispersion relation of bulk SiC has been carried out. Both of these experiments have been limited to the $\Gamma-A$ direction.

In this paper we present an extensive study of dispersion relations of bulk SiC in the 6H-structure. The experimental results will be analysed in the framework of *ab initio* calculations. The paper is structured as follows. A short introduction to the SiC system including structure, symmetry, and group-theoretical aspects (with emphasis on the 6H structure) is given in Section 2. In Section 3 we present our experimental setup and the results of the measurements for the $\Gamma-A$ and $\Gamma-M$ directions. A comparison with theoretical data is presented in Section 4.

2 The SiC System

2.1 Structure of SiC

Silicon carbide develops hexagonal bilayers of silicon and carbon. The various polytypes arise from different stacking sequences of these bilayers. The SiC polytypes belong either to the cubic, hexagonal, or rhombohedral crystal system.

In our experiment we have investigated 6H-SiC at 12 K. The hexagonal 6H structure (C_{6v}^4) consists of 6 bilayers stacked in the order $ABCACB$ along the hexagonal axis. The primitive cell of the crystal lattice is spanned by primitive lattice vectors $\mathbf{a}_i$ with $|\mathbf{a}_1| = |\mathbf{a}_2| = a = 3.077$ Å and $|\mathbf{a}_3| = c = 15.177$ Å at this temperature. The basis of the crystal structure with 6 Si atoms and 6 C atoms can be described with the help of vectors $\mathbf{R}$ pointing to Si

[a] e-mail: dorner@ill.fr

Table 1. Coordinates of basis atoms in 6H-SiC.

Atom	Layertype	Position
Si1	A	$u = 0$
Si2	B	$v = \frac{4}{24}$
Si3	C	$w = \frac{8}{24}$
Si4	A	$u = \frac{12}{24}$
Si5	C	$w = \frac{16}{24}$
Si6	B	$v = \frac{20}{24}$
C1	A	$u = \frac{3}{24}$
C2	B	$v = \frac{7}{24}$
C3	C	$w = \frac{11}{24}$
C4	A	$u = \frac{15}{24}$
C5	C	$w = \frac{19}{24}$
C6	B	$v = \frac{23}{24}$

or C atoms in the A, B, C bilayers,

$$\mathbf{R}_A = u\,\mathbf{a}_3, \quad \mathbf{R}_B = \frac{2}{3}\,\mathbf{a}_1 + \frac{1}{3}\,\mathbf{a}_2 + v\,\mathbf{a}_3,$$
$$\mathbf{R}_C = \frac{1}{3}\,\mathbf{a}_1 + \frac{2}{3}\,\mathbf{a}_2 + w\,\mathbf{a}_3. \qquad (1)$$

The parameters u, v, and w for 6H-SiC are given in Table 1. The Brillouin zone of 3C-SiC and of 6H-SiC including some high-symmetry points is presented in Figure 1.

During the discussion of our results we will repeatedly refer to the 2H and 3C polytypes which feature less atoms per primitive unit cell than 6H. 2H denotes a hexagonal structure with 2 molecular units per unit cell (hexagonal stacking AB). The length of its c-axis is $c(2\mathrm{H}) \approx \frac{1}{3}c(6\mathrm{H})$. 3C stands for the zincblende structure with one molecular unit per primitive cell (hexagonal stacking ABC). The interlayer spacing is almost the same for all polytypes; observed relative differences are of the order of 10^{-3}.

Figure 2 shows a plane in reciprocal space with Brillouin zones both of the 3C (full lines) and 6H structure (dashed lines). The stacking is along the cubic [111] direction. In the description of the cubic crystal, one finds the Γ points of 6H at

$$\mathbf{Q}(\Gamma_n) = \frac{n}{6}(1,1,1)_{3\mathrm{C}} \qquad (2)$$

(in units of $2\pi/a_{3\mathrm{C}}$) with $n = 0, \pm 1, \pm 2, 3$, whereas the hexagonal $\Gamma{-}M$ direction becomes $[\xi\ \xi\ 2\bar{\xi}]$ (or one of its six equivalent directions) in cubic notation with $0 \le \xi \le \frac{1}{3}$, see Figure 2. Note that in the plane of reciprocal space normal to the cubic $[1, \bar{1}, 0]$ direction, shown in Figure 2, six hexagonal Brillouin zones cover the same area as one cubic zone.

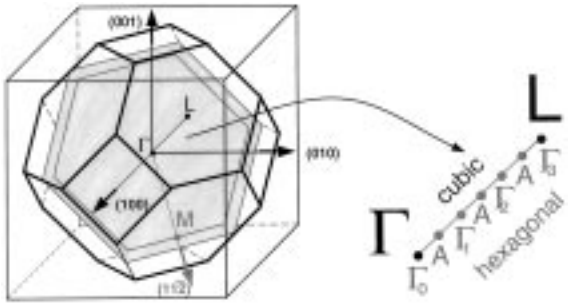

Fig. 1. The cubic 3C-SiC Brillouin zone in three dimensions including some high symmetry points. The grey area shows the cut through the origin perpendicular to the cubic [111] direction. In this cut the larger hexagon represents the limits of the cubic Brillouin zone, while the smaller hexagon corresponds to the limits of the 6H-SiC Brillouin-zone (compare Fig. 2). A three-dimensional section of the 6H-SiC Brillouin zone, including high symmetry points, is indicated by the grey solid lines.

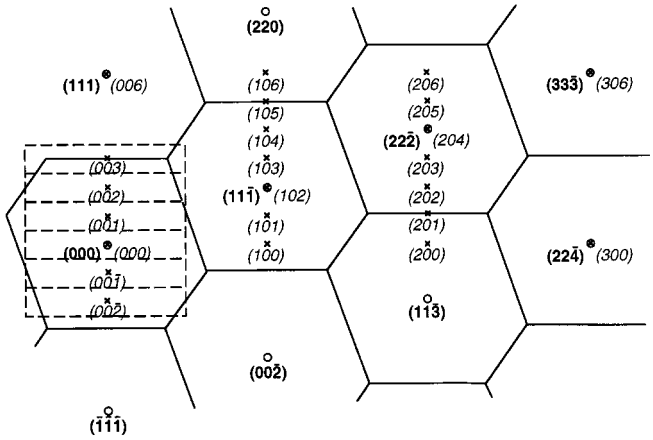

Fig. 2. The experimental scattering plane in reciprocal space perpendicular to the cubic $[1\bar{1}0]$ direction. Brillouin zone centers are given in terms of roman digits for the cubic 3C and by italics for the hexagonal 6H structure. The Brillouin-zone boundaries are depicted by full lines for 3C and by dashed lines for 6H.

2.2 Irreducible representations

A group-theoretical analysis of the $\Gamma{-}A$ direction in 6H-SiC, including the Γ- and A-points, gives six irreducible representations, two of which are twofold degenerate. The dynamical matrix decomposes according to four of these representations: two non-degenerate (each with 6 modes) and two twofold degenerate representations (each with 12 modes). Due to time-reversal symmetry in this nonsymmorphic space group additional degeneracies appear

at the zone boundary (A-point). Two dispersion curves, either non-degenerate or twofold degenerate, join at the A-point with opposite slope to produce twofold or fourfold degeneracy, respectively.

Along the $\Gamma-M$ direction the dispersion relations may be classified according to two non-degenerate irreducible representations: one with 12 modes, the other with 24 modes. At the M-point, there are four representations, again without degeneracy.

3 Experiment

3.1 Instrument and sample

The INS measurements have been performed on the IN1 three-axis neutron spectrometer situated at the hot source of the Institut Laue-Langevin. We have used a Cu(220) monochromator combined with a Cu(200) analyzer. The collimation was 25′, 60′, 60′, 60′. Constant-Q scans have been carried out with a fixed final wave vector at $k_F = 5.0$, 5.75, and 6.8 Å^{-1}. Depending on k_F and the energy transfer the energy resolution has varied between 3 and 11 meV while the Q-resolution was about 0.2 Å^{-1}. Figure 2 shows the experimental scattering plane in reciprocal space.

Our sample was a block of crystalline SiC with dimensions $20 \times 40 \times 2$ mm^3 and a weight of 5.3 g. Calculated Bragg intensities for the three polytypes 6H, 3C, and 2H are listed in Table 2. Although the symmetry of the bulk material is identified as 6H small contributions from the 3C as well as from other unidentified polytypes have been present in the diffraction pattern.

3.2 Results: The $\Gamma-$A direction

The complete set of dispersion curves could be determined by constant-Q scans. The result is presented in Figure 3 in an extended-zone scheme, for clarity. As can be seen, the phonon spectrum of 6H-SiC exhibits a clear gap between 76 and 95 meV. In the following discussion we will profit from this fact and refer to the modes below and above the gap as the "acoustic" and "optical" band, respectively. This phrasing is rigorously correct for the 3C structure, where only three acoustic and three optical modes exist. In the 6H structure, there are six times as many phonon branches due to the increased number of atoms in the unit cell. The 18 branches of the "acoustic" band of 6H-SiC can be considered as the backfolded branches of the 3 genuinely acoustic modes of 3C-SiC, and likewise for the branches of the "optical" band.

A reliable identification of the modes is made possible through the combination of: (i) sufficiently good energy resolution, (ii) measurements in different Brillouin zones, and (iii) "longitudinal" and "transverse" measurement geometries. The modes with longitudinal character, denoted "L" in Figure 3, could be observed from (0 0 24) to (0 0 27) for the "acoustic" band and from (0 0 27) to (0 0 30) for the "optical" band. The doubly degenerate modes with transverse character (denoted "T") have been found from (3 0 0) to (3 0 3) and from (3 0 3) to (3 0 6) for the acoustic and optical bands, respectively, see Figure 2.

Table 2. Cross section of Bragg peaks for different structures normalized to one Si- and one C-atom, with $4\pi(b_{\mathrm{Si}} + b_{\mathrm{C}})^2 = 14.47$, $4\pi(b_{\mathrm{Si}} - b_{\mathrm{C}})^2 = 0.78$ and $4\pi({b_{\mathrm{Si}}}^2 + {b_{\mathrm{C}}}^2) = 7.71$ barn. The Miller indices correspond to the 6H, 3C and 2H structures, respectively. Every row of the table corresponds to exactly one position in reciprocal space. Note that the $(10l)$ Bragg intensities are an even function of l for 2H and 6H but not for 3C. The measurement of a sequence like $(10l)$ therefore allows an easy identification of cubic contaminations. Due to extinction processes this identification can unfortunately not be done on a quantitative basis.

6H		3C		2H	
(1 1 0)	14.47	(0 2 $\bar{2}$)	14.47	(1 1 0)	14.47
(0 0 3)	0	($\frac{1}{2}$ $\frac{1}{2}$ $\frac{1}{2}$)	0	(0 0 1)	0
(0 0 6)	7.71	(1 1 1)	7.71	(0 0 2)	7.71
(0 0 12)	0.78	(2 2 2)	0.78	(0 0 4)	0.78
(0 0 24)	14.47	(4 4 4)	14.47	(0 0 8)	14.47
(3 0 0)	14.47	(2 2 $\bar{4}$)	14.47	(3 0 0)	14.47
(3 0 1)	0	($\frac{13}{6}$ $\frac{13}{6}$ $\frac{2\bar{3}}{6}$)	0	(3 0 $\frac{1}{3}$)	0
(3 0 2)	0	($\frac{7}{3}$ $\frac{7}{3}$ $\frac{\bar{11}}{3}$)	0	(3 0 $\frac{2}{3}$)	0
(3 0 3)	0	($\frac{5}{2}$ $\frac{5}{2}$ $\frac{\bar{7}}{2}$)	0	(3 0 1)	0
(1 0 $\bar{4}$)	0.20	(0 0 $\bar{2}$)	0.78	(1 0$\frac{\bar{4}}{3}$)	0
(1 0 $\bar{3}$)	0.94	($\frac{1}{6}$ $\frac{1}{6}$ $\frac{\bar{11}}{6}$)	0	(1 0$\bar{1}$)	2.11
(1 0 $\bar{2}$)	1.93	($\frac{1}{3}$ $\frac{1}{3}$ $\frac{\bar{5}}{3}$)	0	(1 0 $\frac{\bar{2}}{3}$)	0
(1 0 $\bar{1}$)	1.05	($\frac{1}{2}$ $\frac{1}{2}$ $\frac{\bar{3}}{2}$)	0	(1 0 $\frac{\bar{1}}{3}$)	0
(1 0 0)	0	($\frac{2}{3}$ $\frac{2}{3}$ $\frac{\bar{4}}{3}$)	0	(1 0 0)	3.66
(1 0 1)	1.05	($\frac{5}{6}$ $\frac{5}{6}$ $\frac{\bar{7}}{6}$)	0	(1 0$\frac{1}{3}$)	0
(1 0 2)	1.93	(1 1 $\bar{1}$)	7.71	(1 0$\frac{2}{3}$)	0
(1 0 3)	0.94	($\frac{7}{6}$ $\frac{7}{6}$ $\frac{\bar{5}}{6}$)	0	(1 0 1)	2.11
(1 0 4)	0.20	($\frac{4}{3}\frac{4}{3}\frac{\bar{2}}{3}$)	0	(1 0 $\frac{4}{3}$)	0

As will be pointed out below, the dispersion relation along the $\Gamma-A$ direction in 6H-SiC in a first approach, *i.e.*, omitting changes in the interaction potentials, can be linked to the one of 3C-SiC by the mechanism of backfolding, see Figure 2. From the group-theoretical results of Section 2.2 we know that the phonons at the Γ-point have the same symmetries as those along the $\Gamma-A$ direction. This implies that the additional degeneracies introduced by backfolding have to be lifted by the opening

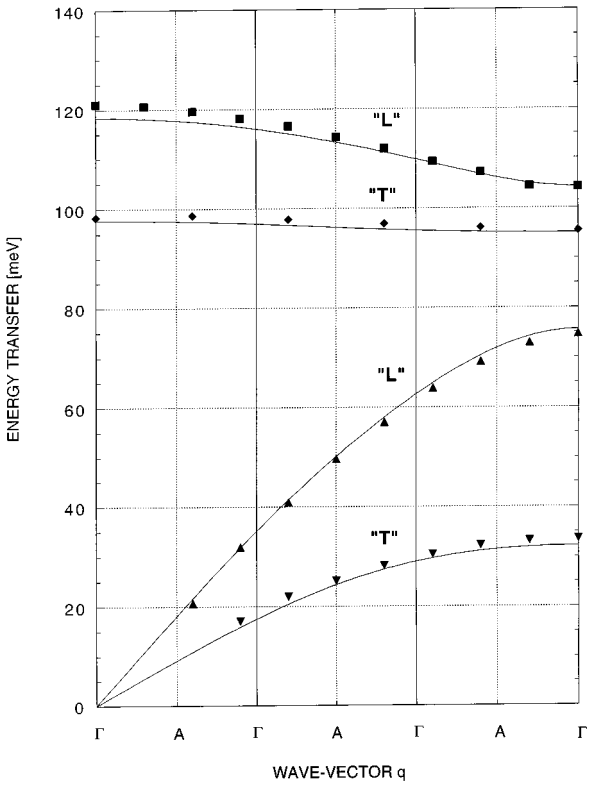

Fig. 3. Phonon dispersion relation for the $\Gamma-A$ direction in an extended-zone scheme. Experimental data points and theoretical lines from 3C *ab initio* calculations by Karch *et al.* [9].

of gaps at the two "inner" Γ-points ($n = \pm 1$ or $n = \pm 2$ in Eq. (2)) in the extended zone-scheme of Figure 3. These gaps have been determined by Feldman *et al.* [7] using Raman spectroscopy to be in the range of 0.5 to 1 meV. We have not been able to resolve these small splittings. In fact, we have not performed scans at the "inner" Γ-points ($n = \pm 1, \pm 2$ in Eq. (2)), but very close to them along the $\Gamma-M$ direction. The absence of strong splittings indicates that the phonons with wavevector perpendicular to the bilayers exhibit little sensitivity to the specific stacking sequence.

3.3 Results: The $\Gamma-$M direction

As a comprehensive understanding of the lattice dynamics cannot be based on one symmetry direction only, we have pursued our investigations along the $\Gamma-M$ direction which is perpendicular to $\Gamma-A$. The results are summarized in Figure 4. The data points are connected through spline interpolation curves to guide the eye and to present an identification of the modes as explained below.

Due to the symmetry of the eigenvectors the 12 modes belonging to one of the irreducible representations are rigorously invisible (*i.e.*, they have a vanishing one-phonon scattering cross-section) in our experimental setup, in which the momentum transfer Q lies within one of the mirror planes of the 6H-structure. This selection rule strongly facilitates the task of identifying the experimental signals

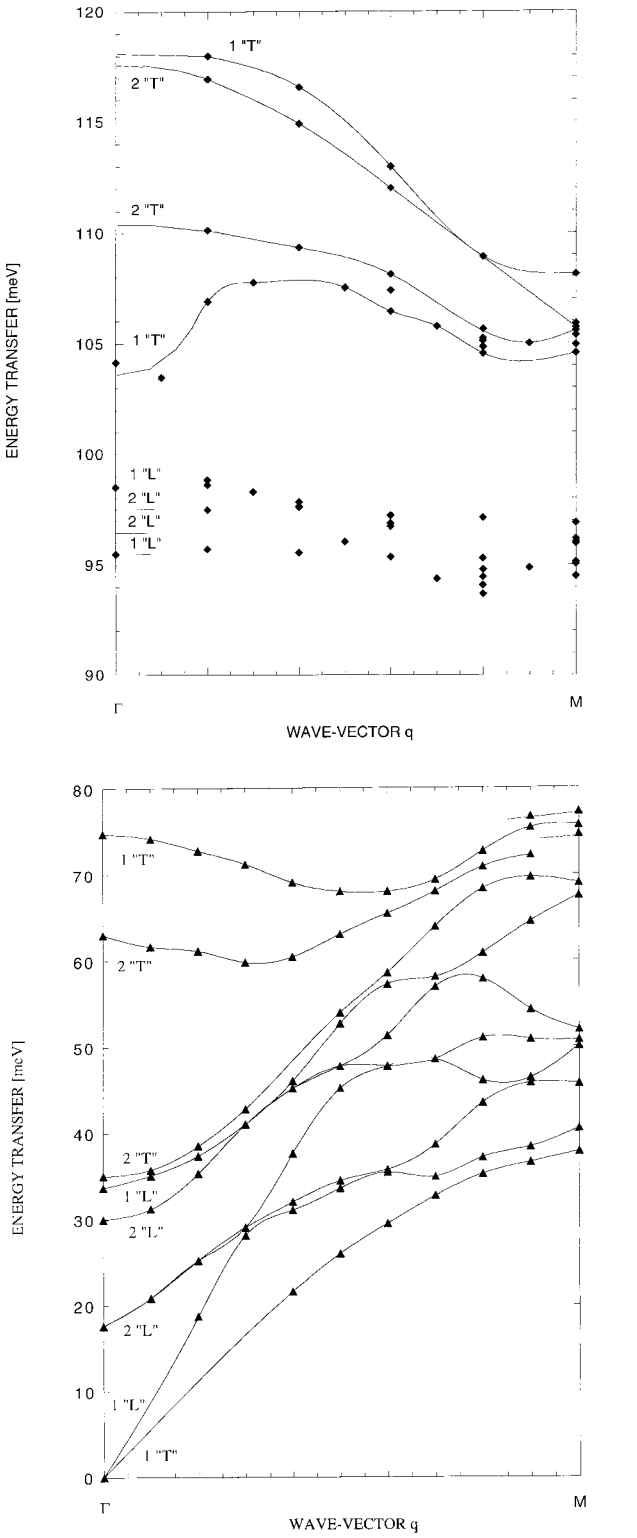

Fig. 4. Phonon dispersion relation for the $\Gamma-M$ direction. The measured data points are interpolated by spline curves to guide the eye and to represent our identification of different modes. Numbers and symbols, indicating "longitudinal" and "transverse" character of the modes, on the right-hand side of the energy axis refer to the number and characters of visible modes leaving the Γ-point, as known from the measurement of the $\Gamma-A$ direction.

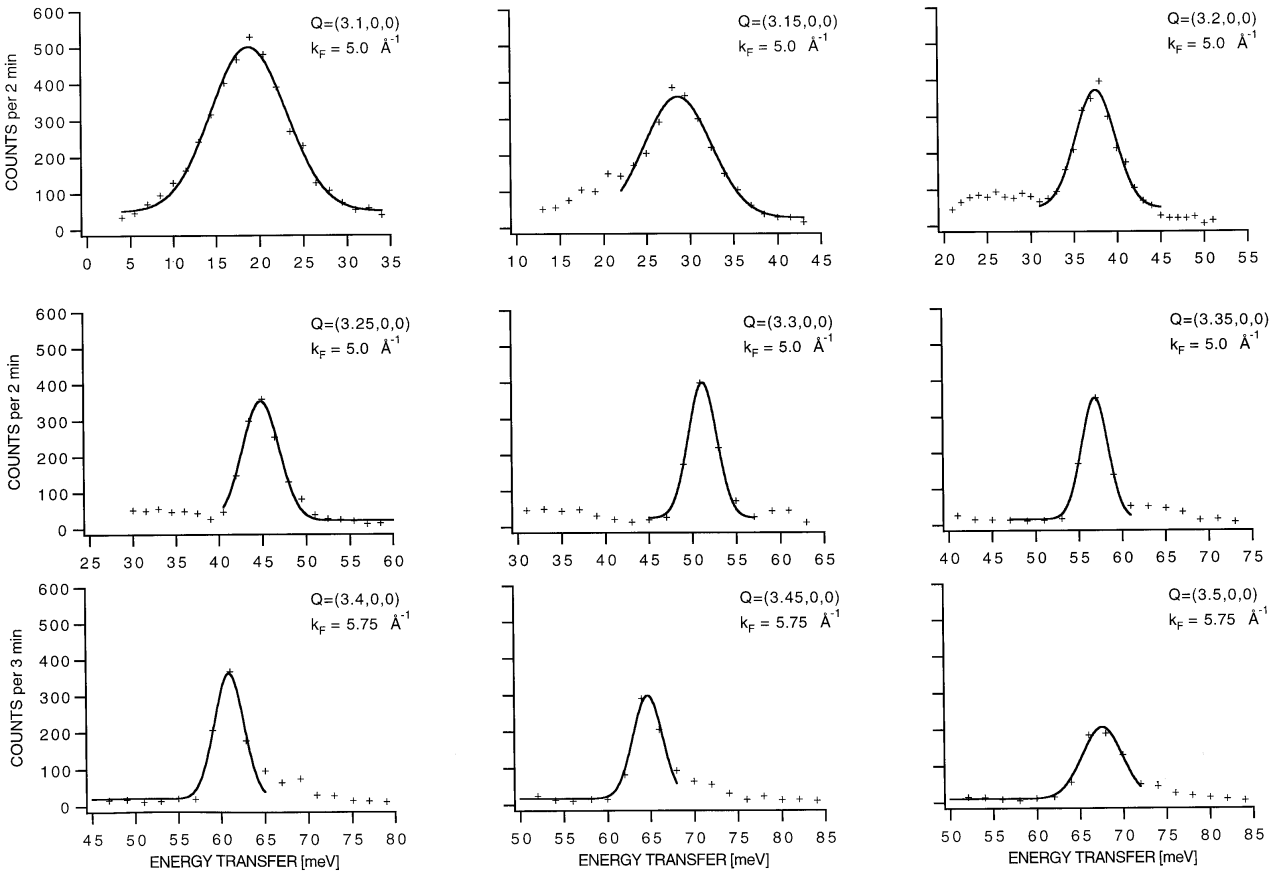

Fig. 5. Constant-Q scans observing the "longitudinal acoustic" mode character through several anticrossings.

with the dispersion branches of the crystal. Thus, we expected to observe a maximum of 24 modes. Each of these modes belongs to the same representation which leads to an anticrossing of all the visible modes. The intersection of some of the splines in Figure 4 is just an artifact of the interpolation and has no physical origin.

Apart from the LO–TO splitting (see below), the phonon branches connect at the Γ-point, and we can use our rather complete knowledge of the dispersion relation along $\Gamma{-}A$ to infer the number and character of branches along $\Gamma{-}M$ starting at Γ: one "longitudinal" plus two "transverse" modes at the "outer" Γ-points ($n = 0$ or $n = 3$ in Eq. (2)) and two "longitudinal" plus four "transverse" modes at the "inner" Γ-points ($n = \pm 1$ or $n = \pm 2$) in the extended-zone scheme. Note that half of the twofold degenerate "transverse" modes along the $\Gamma{-}A$ direction are invisible in our scattering geometry. Along $\Gamma{-}M$, these degeneracies are lifted, *i.e.*, each doubly degenerate "transverse" mode of the $\Gamma{-}A$ direction connects to one visible "longitudinal" and one invisible "transverse" mode along $\Gamma{-}M$. The number of visible modes and their polarization as infered from the $\Gamma{-}A$ direction is given by the symbols on the right-hand side of the energy axis in Figure 4. For example, the notation 2 "L" indicates that we expect at this energy two slightly split modes with longitudinal character.

While near the Γ-point the identification of the measured signals is reliable this is no longer the case when approaching the M-point. The energy resolution of the instrument was insufficient to clearly resolve the close-lying signals. Therefore, insight into the character of the modes is impossible without an interpretation of the scattering intensity. The 6 lowest-frequency modes at the M-point have been observed at (0.5 0 l) with $l = 24$, 25, 26, 25, 26, 27 in the order of increasing frequency. They apparently have "transverse" character, and the modes of the lowest and the highest frequency of this "transverse" group connect to single modes (1 "T") at small q.

Experimentally we have been able to follow the longitudinal "acoustic" branch from low frequencies, where the dispersion is linear and the mode is correctly called acoustic, through several anticrossings along the [3 + ξ 0 0]-direction. Figure 5 shows a series of constant-Q scans with signals from this mode. The widths of the signals reflect focussing in reciprocal space. With increasing energy transfer, *i.e.* with increasing incoming energy, the resolution ellipsoid of the instrument orients more parallel to the dispersion curve giving better focussing. This favorable turning of the resolution ellipsoid as a function of incoming energy also explains why the change from $k_F = 5.0$ Å^{-1} to $k_F = 5.75$ Å^{-1} only leads to a comparatively weak broadening of the signal. At the zone boundary (3.5 0 0) this single mode ends up at 68 meV,

which is the lowest-frequency mode of the "longitudinal" group of 6 expected modes. The three highest-frequency modes of this group have been observed in transverse geometry in three different Brillouin zones, at (0.5 0 25), (0.5 0 26) and (0.5 0 27) from lowest to highest frequency. Unfortunately, we have not been able to clearly follow the corresponding intensities in the interior of the Brillouin zones. We are, therefore, not fully convinced that we have identified all six modes in this group.

For the "optical" band we have obtained intensities from the "longitudinal" modes in various Brillouin zones without a clear identification as to which mode was responsible for the intensities. The experiment does not supply sufficient indications as how to draw the dispersion curves.

The "transverse" modes in the "optical" band could be identified more clearly. From low to high frequencies they have been observed at [ξ 0 27], [ξ 0 28], [ξ 0 29], and [$3 + \xi$ 0 12]. The band due to the mode with the highest frequency at [ξ 0 30] was very weak. Thus, we have observed the two 1 "T" and the two 2 "T" modes and their dispersion at small values of ξ. But near the M-point the 6 expected modes could not be identified.

In summary, near the M-point there is a total of 18 modes in the "acoustic" band, 12 of which are visible in the given scattering geometry, and 10 of the 12 have been identified. In the "optical" band, again featuring 18 modes, only 4 out of 12 visible modes could be identified near the M-point.

So far we have not discussed the possible splitting of longitudinal and transverse optical modes as a consequence of the macroscopic electric field generated by the effective charges of Si and C. We have observed indeed such an LO–TO splitting in the case of the highest-frequency optical mode. The highest optical mode in the $\Gamma-A$ direction, which has longitudinal character, joins the Γ-point at 121 meV. By extrapolation of the highest mode in the $\Gamma-M$ direction, which has transverse character, we find a value of about 118 meV at the Γ-point. It is reasonable to assume that both modes without macroscopic field would connect at the Γ-point and that the difference is due to the LO–TO splitting. In the case of all the other modes we do not see such a splitting.

4 Comparison with theory

4.1 Relation between 3C- and 6H-dispersion curves

In order to get a better understanding of the interactions in SiC we have compared our experimental results with theoretical calculations. An *ab initio* determination [9] of the phonon dispersion relation exists only for the 3C structure.

If one neglects the difference between the force constants of the $ABCABC$ (3C) and the $ABCACB$ (6H) stacking, the dispersion sheets of the 6H-structure would be a compilation of the six sets of cubic 3C dispersion sheets with Γ-points Γ_n ($n = 0, \pm 1, \pm 2, 3$). For the $\Gamma-A$ direction this is equivalent to the procedure of "backfolding" known from superlattice structures. For the $\Gamma-M$ direction this procedure resembles the construction of the quasi-continuum of phonons in thin-film structures.

The apparent degeneracies of the modes ($n = 1, 2$) at the 6H zone center which result from folding are lifted by the actually different force constants in the two different structures.

4.2 The $\Gamma-$A direction

The lines in Figure 3 represent the theoretical results for the $\Gamma-A$ direction obtained according to the previous section, *i.e.*, they show the 4 genuine dispersion curves of 3C-SiC, representing two "L" and 2 doubly degenerate "T" branches. In this way, one generates the 12 dispersion curves of the "acoustic" and "optical" band of 6H-SiC, respectively, where the "T" modes remain doubly degenerate.

Although the calculations and experiments have been done for different polytypes, there is good agreement between them. Therefore, the frequencies of phonons with a wavevector perpendicular to the bilayers depend only weakly on the stacking sequence. This insensitivity was already evoked in context with the small gaps at the "inner" Γ-points.

4.3 The $\Gamma-$M direction

By equation (2) we have defined points in the Brillouin zone of the cubic 3C structure which correspond to Γ-points in the hexagonal 6H structure. Now we extend this concept and define the lines $\mathbf{Q}_n(\xi)$ in the cubic Brillouin zone which correspond to the phonon wave vectors $\mathbf{q}(\xi)$ of the $\Gamma - M$ direction in 6H, written in cubic coordinates:

$$\mathbf{Q}_n(\xi) = \frac{n}{6}(1,1,1)_{3C} + \mathbf{q}(\xi),\ n = 0, \pm 1, \pm 2, 3 \qquad (3)$$

with

$$\mathbf{q}(\xi) = \xi(1,1,\bar{2})_{3C}. \qquad (4)$$

The resulting dispersion curves are shown in Figure 6 where we present the visible modes along $\Gamma-M$. The six different lines $\mathbf{Q}_n(\xi)$, see equation (3), produce 6 different sets of dispersion curves each. The fact that the sets for $n = 1, 2$ are different from the sets for $n = -1, -2$ can be visualized by inspecting Figure 2. The 24 visible modes (out of 36) in the 6H structure are now predicted on the basis of the six times four corresponding modes of the 3C structure. The apparent degeneracies at $\mathbf{q} = 0$ are an artifact due to the calculation on the basis of the cubic 3C structure. In 6H these modes must show a gap, as explained already above.

We observe good agreement between calculation and experiment from the Γ-point to up about half way through the Brillouin zone. This comes as no surprise given the

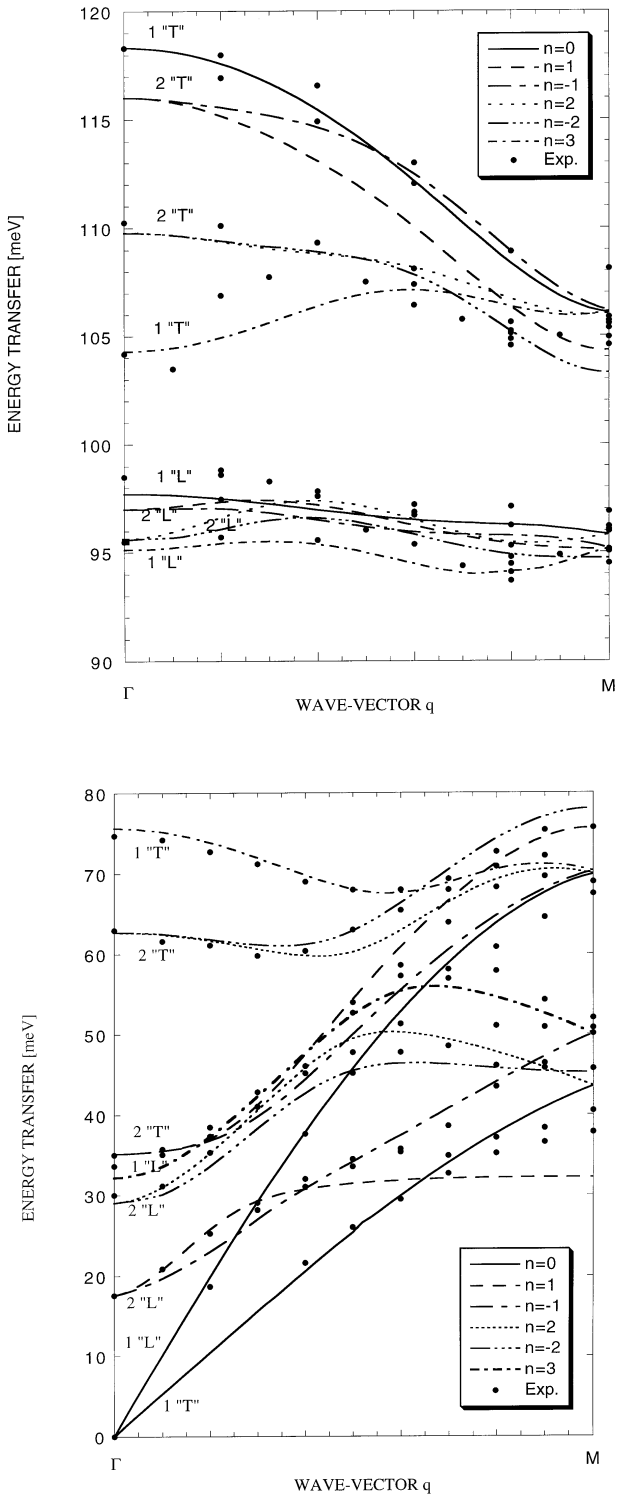

Fig. 6. Measured data points of the phonon dispersion relation in the $\Gamma-M$ direction and backfolded dispersion relations of the 3C structure, taken from Karch *et al.* [9]. Numbers and symbols on the right-hand side of the energy axis have the same meaning as in Figure 4. The different styles correspond to different lines $\mathbf{Q}_n(\xi)$ as defined in equation (3).

Table 3. Parameters for the rigid-ion model with Born-von Karman forces and effective charges.

	Si–C	Si–Si	C–C
longitudinal force constant [N/m]	233.39	23.13	11.07
transverse force constant [N/m]	11.51	2.416	1.895
		Si	C
effective charge [e_0]		1.012	−1.012

good agreement for the $\Gamma-A$ direction. But apparent discrepancies occur near the M-point. The discrepancies have to be attributed to the subtle differences in the atomic interactions stemming from the actually different stacking sequences of the two structures.

The discrepancies can be partially rationalized by symmetry considerations: the 6 types of branches in Figure 6 have their origin in completely different lines $\mathbf{Q}_n(\xi)$ of the Brillouin zone of 3C, see equation (3), and therefore cross when simply transposed to 6H. In the actual 6H structure such crossings are forbidden by symmetry, since all visible modes belong to the same representation. This leads to anticrossing and related gaps in the experimental curves.

Thus, the 3C-based theoretical data cannot be expected to give more than a semi-quantitative understanding of the measured 6H dispersion. Calculations based on the actual 6H structure are necessary in order to correctly include the above-outlined symmetry-related features. However, due to the complexity of the 6H-SiC structure with 12 atoms per primitive cell *ab initio* calculations are extremely expensive. An easier solution consists in mapping the *ab initio* calculations [9] of 3C-SiC onto a rigid-ion model which is then readily transposed to the more complex 6H-structure. We have opted for a simple model containing only Si–C, Si–Si, C–C nearest-neighbor interactions. Coulomb interaction between the effective charges (*i.e.*, Born's effective charge divided by the high-frequency dielectric constant) of Si and C are also included. The values for the parameters are displayed in Table 3. Using this model, we have calculated dispersion curves and phonon intensities. It turns out that due to its simplicity the model does not lead to a quantitatively improved description of the dispersion relation with the rigid-ion model as compared to the *ab initio* calculations for 3C-SiC. However, the calculated phonon branches now show the typical features (anti-crossings *etc.*) of the experiment. This confirms that the symmetry (or stacking sequence) influences the dispersion curves *via* the mechanisms outlined above even without changes in the interatomic interactions themselves. Except for modes close to the M-point in the region from 65 to 80 meV, the calculated and measured intensities agree well. Therefore, these model calculations give us further confidence in the correctness of our assignments.

5 Conclusion

Using inelastic neutron scattering we have investigated the phonon-dispersion relation of 6H-SiC along the $\Gamma-A$ and $\Gamma-M$ directions. In the $\Gamma-A$ direction the complete set of modes could be determined. In the $\Gamma-M$ direction we have been able to identify 14 out of 36 modes. When comparing the experimental data with *ab initio* calculations based on the cubic 3C structure good agreement is found for the $\Gamma-A$ direction. This implies: (i) the *ab initio* calculations correctly describe the dynamics of the 3C-SiC system, and (ii) the modes with a modulation vector perpendicular to the bilayers are rather insensitive to the change in interatomic interactions occasioned by the stacking periodicity. That the phonon dispersion relations are actually influenced by this periodicity is demonstrated by the comparison of theory and experiment for the $\Gamma-M$ direction. There we find a considerably worse agreement with the *ab initio* calculations, *i.e.*, the simple transposition of dispersion relations from 3C to 6H fails. This failure constitutes strong evidence for a dependence of the dynamical response of the SiC system on the stacking sequence. Either direct experiments or further *ab initio* calculations on other SiC types are desirable to corroborate this finding which, in the light of the very similar static electronic energies, may be of considerable relevance for the understanding of polytypism in SiC.

References

1. G. Pensl, R. Helbig, in *Festkörperprobleme/Advances in Solid State Physics*, edited by U. Rössler (Braunschweig, Vieweg, 1990), Vol. 30, p. 133, and references therein.
2. A.R. Verma, P. Krishna, *Polymorphism and Polytypism in Crystals* (Wiley, New York, 1966).
3. N.W. Jepps, T.F. Page, Prog. Cryst. Growth Charact. **7**, 259 (1984).
4. G.C. Trigunayat, G.K. Chada, Phys. Stat. Sol. A **4**, 9 (1971).
5. B. Winkler, M.T. Dove, E.K.H. Salje, M. Leslie, B. Palosz, J. Phys.-Cond. **3**, 539 (1991).
6. C. Cheng, V. Heine, I.L. Jones, J. Phys.-Cond. **2**, 5097 (1990).
7. D.W. Feldman, J. Parker, W.J. Choyke, L. Patrick, Phys. Rev. **170**, 698 (1968); *ibid.* **173**, 787 (1968).
8. G. Lorenz, H. Boysen, F. Frey, H. Jagodzinski, G. Eckold, *Akustische Phononen in SiC*, Neutronenspektrometer UNIDAS, Ergebnisbericht 81-86, Juel-Spez-410, p. 39 (1987).
9. K. Karch, P. Pavone, W. Windl, O. Schütt, D. Strauch, Phys. Rev. B **50**, 17054 (1994); K. Karch, Ph.D. thesis, University of Regensburg, 1993.